Experimental and Computational Studies in Far-from-equilibrium Systems like Rayleigh-Bénard Convection

by

Yash Yadati

A Major Qualifying Project

Submitted to the Faculty

of the

WORCESTER POLYTECHNIC INSTITUTE

In partial fulfillment of the requirements for the

Degree of Bachelor of Science

in

Physics and Mechanical Engineering

by

May 2020

APPROVED:

Professor Germano S. Iannacchione, Major Thesis Advisor

Professor Robert Daniello, Major Thesis Advisor

Abstract

Lets look at a combustion engine, which in the most literal sense is designed to exploit the Second law of Thermodynamics. Take a glass of petrol, it is in an ordered form of energy by itself but when the petrol is ignited in a combustion engine, the volume increases (not to mention the heat and sound dumped onto the environment) and the once ordered energy becomes disordered. The combustion engine is special in that it can harness the dissipating energy and tap in to the flow of heat and use it to create a small pocket of order to run it's pistons in the midst of all that disorder. Combustion engines are not the only ones, even life itself does this. When you receive energy in the form of food, your body processes the ordered energy and converts it in to more disordered energy but it uses the proceeds off it to power itself. All the while the entropy of the universe is constantly increasing. In fact, we see this all around us, from crack propagation in materials to phase and glass transitions, from inter-cellular transportation at the nano-scale that form the basis of life to the weather systems that dictate the movement of the water, carbon and nitrogen cycles of our planet [7]. There is unifying theme that comes across from this and that is, there is a high level of complexity that emerges spontaneously in these systems. Classical equilibrium thermodynamics cannot answer this and is therefore rendered insufficient in explaining the underlying dynamics that allow for such complexity. In this report, we study one such system, the steady-state Rayleigh-Bénard Convection. An important observation we were able to see through the current study was how temperature took on a time independent trait yet maintained a spatially varying character. Our study employs a unique technique by using an Infrared camera to extrapolate thermal profiles and present it statistically. On a further note, the report also discusses the different approaches that can be adapted to extend the current study to turbulence, complex networks and information theory.

Contents

1 Introduction

Since the 1700s, classical thermodynamics has fundamentally changed the way we live and how we solve issues in the real world due to its universality in explaining the flow of energy. However, the basis of such explanations are grounded on the idea that the systems are closed and in a state of thermodynamic equilibrium [25]. As we now know, almost all systems are open to constant influxes of energy and matter and its impossible to separate or completely close a system from the rest of the universe and therefore almost no system is in equilibrium. The current challenge in Statistical Thermodynamics is to explain these "non-equilibrium" systems and their processes. Most of the current theories attempt to approximate these non-equilibrium systems from an equilibrium thermodynamics perspective but such theories are limited by equilibrium thermodynamics itself [2, 7, 1]. In this report we explore experimental and computational techniques that can be used to understand such far-from-equilibrium systems and help build a general theory in the future. We use a prototype system, the Rayleigh-Bénard Convection, to do this.

1.1 Equilibrium Thermodynamics

In the past couple of centuries, scientists have come to understand that energy drives the universe through the laws of thermodynamics. In general, a hotter object (concentrated energy source) would leak energy to its surroundings in the form of heat. A heat engine, in the modern sense, takes advantage of this process by tapping in to the flow of heat to do useful work. Although, work (mechanical form) and heat are two very different concepts they are faucets of the same thing, energy. This is usually expressed mathematically in the form of the First Law of Thermodynamics, written as so:

$$dU = \delta Q - \delta W \tag{1}$$

where dU is the change in internal energy of the system, δQ is amount of energy supplied to the system by a heating process and δW is the quantity of energy lost by the system due to work done by system on the environment. The two kinds of processes that can change the internal energy of a closed system are heat and work and in a very subtle way, this equation tells us that this relationship is conserved. It reveals that energy can never be created nor destroyed but merely transferred from one state to another. The internal energy of the system was later understood to be a state variable expressed in the form of entropy, S and volume, V : $U = U(S, V)$. Temperature, T and pressure, P are partial derivatives of $U(S, V)$ and all these thermodynamics variables are defined only when the the system is in its own state of internal thermodynamic equilibrium as seen further on.

It is important to recognize that thermodynamics was initially developed with a steam-engine centric view that systems are macroscopic and useful work was some kind of extraction of energy to do mechanical work. As the entire concept of kinetic theory (microscopic particles, like atoms, interacting and transferring heat) picked on, it became impossible to calculate explicitly

the energy and motion for every individual particle and for this reason, thermodynamics takes the general motion of these particles and solves for the average values of the variables (both intensive and extensive: U, W, Q, S, V, T and P), under conditions of equilibrium.

Eventually, the kinetic energy of the particles in a hot object gradually decay as heat flows from the system to the surroundings. Heat is a one way flow of energy and unless work is done on the system or more heat is added to the object, the system will lose its internal energy. This came to be understood through the Second Law of Thermodynamics where:

$$\frac{dS}{dt} \geq 0 \tag{2}$$

In the above equation, t is time, indicating that the rate of change of entropy must never decrease. In time, a closed system will always achieve a state of maximum possible entropy, or in other words, a state of thermodynamic equilibrium [22]. Thermodynamically speaking, it can be deduced from this that the whole process is irreversible and we can never go back in time because symmetry between the previous states and the future states is broken (in a classical sense) [30]. Herein lies the connection to Far-from-equilibrium Thermodynamics, where the internal energy of the system is changing between any two given states.

However, when a system is in equilibrium, it will behave ergodically suggesting that it will carry itself out uniformly in both space and time because the change in internal energy is zero. When this is combined with the first law of thermodynamics, heat can be redefined in relation to temperature and entropy to give:

$$dS = \frac{\delta Q}{T} \tag{3}$$

Adapting the idea of microscopic particles in facilitating the transfer of heat was groundbreaking. Ludwig Boltzmann understood that in order to attempt to formulate such a system with trillions and trillions of particles he had to abandon certainty and instead use concepts of probability to show that atoms could be travelling at certain speeds and directions. This formed the basis of what is now called Statistical Thermodynamics [19]. The main idea of Statistical mechanics is to take the macroscopic system to be a series of events occurring at certain probabilities on the microscopic scale and formulating the two. The probability was found using the partition function ($\mathbb{Z}$) as a normalization constant,

$$p(E) = \frac{e^{-\beta E}}{\mathbb{Z}} \tag{4}$$

Here β is the inverse temperature $1/k_B\mathrm{T}$ where k_B is Boltzmann's Constant and E is total energy of the micro-state. With this thermodynamic variables like entropy can be redefined in terms of the new probability distribution,

$$S = k_B \ln(\mathbb{Z}) \tag{5}$$

$$\bar{E} = -\frac{\partial}{\partial \beta} \ln(\mathbb{Z}) \tag{6}$$

$$\bar{p} = \frac{1}{\beta}\frac{\partial \ln(\mathbb{Z})}{\partial V} \tag{7}$$

This is the probability that the system will be in a certain state as a function of that state's energy. Formally, equation (5) is the thermodynamic definition of entropy and it tells us that entropy is a measure of disorder. The distribution for equilibrium systems, which is widely seen in many fields, is Gaussian and is commonly referred to as a Grand-Canonical Ensemble. It implies that in a state of equilibrium there is uniformity across time and space [20].

1.2 Far-from-equilibrium Thermodynamics

Closed systems or isolated systems will continue to be in a state of equilibrium until and unless they are driven out by an external steady flow of energy. In a statistical sense, equilibrium is associated to a state of randomness across both space and time, implying that there is some sort of symmetry. And although the system is characterized by macroscopic variables like pressure, temperature and volume, from a microscopic point of view, the system will explore all possible states before collapsing into a single point in phase space [25, 6, 12]. This forms the basis of classical thermodynamics. However, when we look around us, almost all systems are open while being driven out by an energy flux.

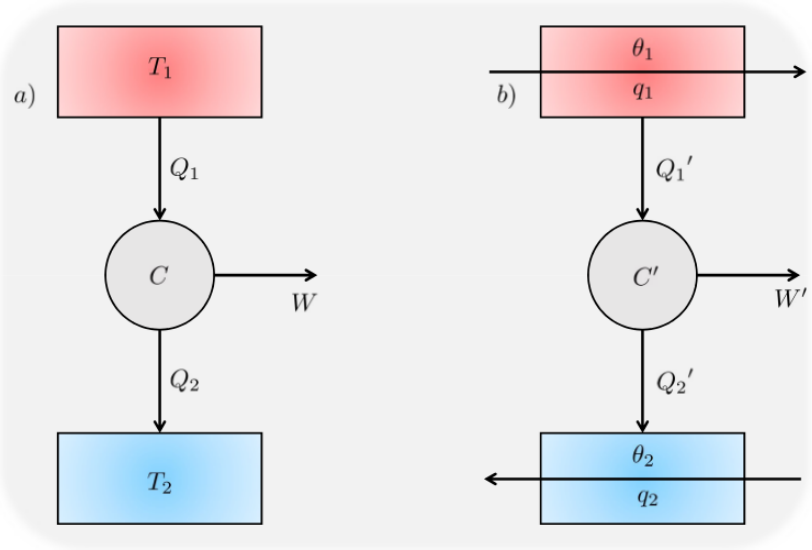

Figure 1: a) Figure shows a theoretical Carnot engine, C, operating between two reservoirs with temperature T_1 and T_2 ($T_1 > T_2$). It derives heat Q_1 from the reservoir kept at T_1, dumps heat, Q_2 into the colder reservoir kept at T_2 while does work, W. b) Figure shows a practical Carnot engine, C', operating between two reservoirs with temperature's θ_1 and θ_2. It is kept at a steady-state by the constant heat influxes, q_1 and q_2. It derives heat Q_1' from the reservoir kept at θ_1, dumps heat, Q_2' into the reservoir kept at θ_2 while doing lesser amount of work, W' ($W' < W$).

A standard approach to dealing with the issue is based on the local equilibrium hypothesis, in which the system can be broken apart in time and space as subsystems where we would then be able to apply to approximation, classical equilibrium thermodynamic conditions [31]. A simple theoretical Carnot engine (C), as seen in Figure 1(a), in a macroscopic sense describes

the efficiency of thermal engines, i.e. the ratio of the work done and the heat coming from the hot reservoir. It does this by averaging these quantities and assuming reversibility. However, it becomes cumbersome to visualize this in reality because no real engine is reversible (there is always positive change in entropy). In order to maintain the reservoirs at constant temperature, a heat flux must be accommodated and maintained for and that is why no practical Carnot engine (C') can remain as efficient as a theoretical Carnot engine (C). The maximum possible efficiency of a theoretical Carnot Engine (C) is now reduced to a function of the steady state non-equilibrium temperature of the reservoirs as seen in Figure 1(b) [2, 14]. In the scientific community, this function is achieved by accounting for the microscopic behavior of the engines, which are subjected to strong fluctuations (Fluctuation Theorem) [16].

The challenge is clear, to be able to apply thermodynamics to these systems we would not only need to reestablish the definitions of the thermodynamic variables but also find ways to quantify the emergent order or complexity, which represents the gap in our understanding of these systems from a thermodynamic point of view [2, 5, 28, 11]. While equilibrium systems exhibit complete randomness, far-from-equilibrium systems are dependent on fluctuations because they are incredibly sensitive to the driving perturbation. Take that glass of petrol again. While a combustion engine can vaporize the petrol quickly, it is however a process that needs a sufficiently high thermal gradient. If you were to heat this glass of petrol over a flame at lower thermal gradients, you will see that it takes time to achieve a thermal gradient adequate enough to establish convection currents within the liquid, without vaporizing it. During this period, hotter less dense liquid flows upwards while the colder more dense liquid drops downwards, in a cycle. The onset of this feature in convection is denoted by the critical value of the dimensionless constant, Rayleigh Number (Ra) [29]. When the thermal gradient is increased like in the combustion engine, the convective motion becomes turbulent and chaotic, this is usually marked by higher values of the Rayleigh Number (Ra $\sim 10^9$ for vertical surface). Convection itself is a by product of far-from-equilibrium systems and in it's very nature there is a high degree of complexity.

In order to begin understanding how complexity arises and how to quantify it we use a prototype system, the Rayleigh-Bénard Convection system.

1.3 Background on Rayleigh-Bénard Convection

A mode of transfer of heat, convection is a type of fluid flow that exists due to the competing forces of viscosity, buoyancy and surface tension. When a fluid is exposed to a non-uniform temperature gradient on a horizontal plane, such as a plate being heated from below, a difference in density changes the dynamics of the fluid, producing convection patterns [26]. This phenomena is known as Rayleigh-Bénard instability. The hotter less dense fluid moves upward and is replaced by the cooler more dense fluid that flows downward. Visually, these can be seen as cells and they join at higher temperatures to form rolls like in Figure 2 [33].

It is an observed feature that systems, such as Rayleigh-Bénard convection, when driven out of equilibrium exhibit complex patterns. These patterns show a spontaneous formation of

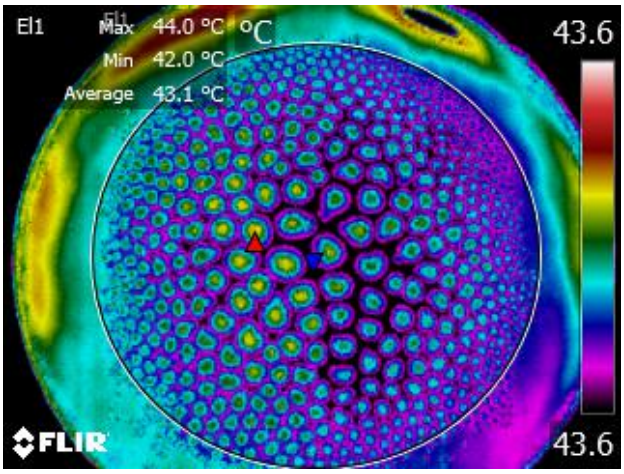

(a) Hexagonal Cells

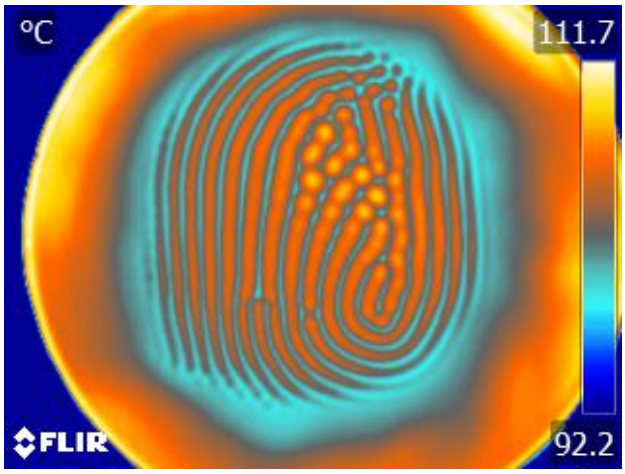

(b) Rolls

Figure 2: Different Patterns observed by performing real time-thermal imaging when silicone oil a) 10 cSt and b) 150 cSt is heated. Note the homogeneity in the structure for 150 cSt

order and develop in time as a function of thermal fluctuations. Like all other driven out-of-equilibrium systems, the patterns evolve and mature at various time and length scales [5, 7]. As mentioned earlier, we use the Rayleigh-Bénard Convection as our prototype system in order to show how far-from-equilibrium systems display complexity. Rayleigh-Bénard Convection is a simple convection system, that arises from a thermal gradient and the patterns represent convective instability as seen in Figure 3. This figure depicts the experimental configuration of the study. A thin layer of fluid is heated from the bottom at constant power ($\dot{Q}$). As convection settles down into a stable state, the liquid at the bottom of the pan which is at temperature, T_{bottom}, becomes time-independent while the temperature at the surface of the liquid (T_{top}) initiates a spatial reordering. This information is extracted by performing real-time thermal imaging from above and, by extrapolating the images we can analyze the statistics behind the thermal fluctuations as a function of both space and time.

The convective instability creates a spatio-temporal non-uniform thermal distribution on the surface of the fluid film as seen in Figure 3. The advantage of this lies in the simplicity of being able to dimensionless parameters. We use one such important parameter from the world of fluid mechanics to understand what kind of liquid we can play around with: the Rayleigh Number (Ra). The Rayleigh Number is a dimensionless quantity that determines the onset of convection. Initially we focus on non-turbulent liquids, so we used liquids that have a low Rayleigh Number. For no-slip boundary conditions (infinite parallel plates), the number is called the critical Rayleigh Number and was calculated to be 1708 by Jeffreys in 1926 [18]. In our experiments we used silicone oil with a viscosity of 150 cSt ($Ra = 2500$ to $Ra = 3500$ with temperatures from $T = 20°C$ to $T = 130°C$) for non-turbulent flows and later extended it to turbulent flows by using glycerol water mixtures ($\text{Ra} > 8 \times 10^4$ with temperatures above $T = 20°C$). For non-turbulent experiments the thickness of the oil was relatively thin, about $4mm$-$5mm$ while this increased to about $1cm$ for turbulent conditions.

Since the critical Rayleigh Number for convective patterns to emerge is around 1708, we can check if our values should show convection without needing to directly recognize the patterns in

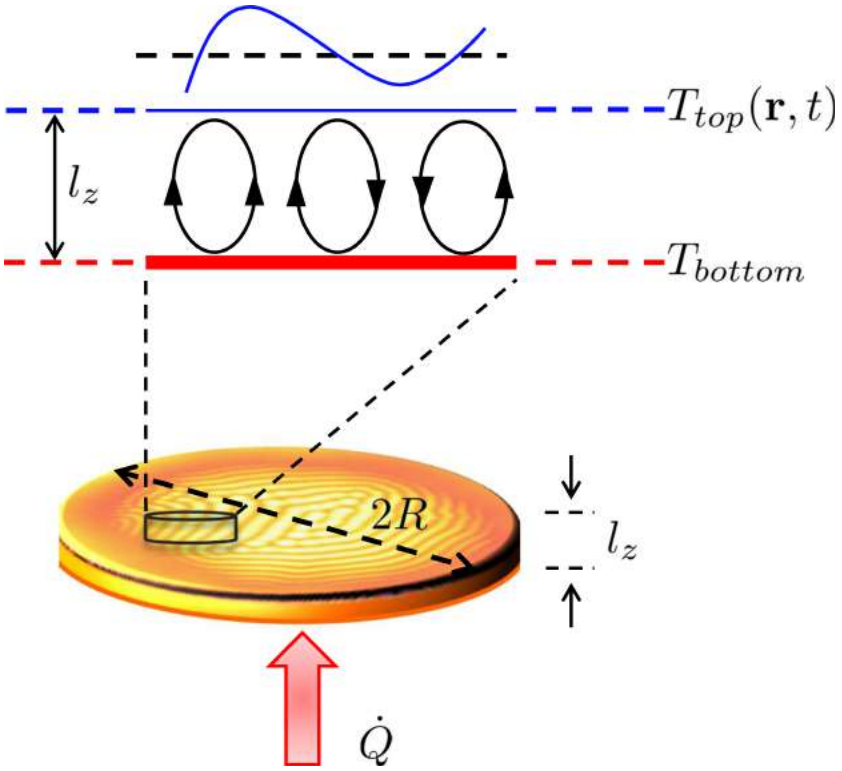

Figure 3: Cartoon illustrates the experimental configuration of the current study. The Rayleigh-Bénard system at steady-state is set up by heating a thin film of viscous liquid from the bottom ($\dot{Q}$). The temperature difference between T_{bottom} and T_{top} gives rise to convection rolls. While at steady-state, T_{bottom} is constant, real-time thermal imaging of the top layer is performed to extract the spatial and temporal distribution of T_{top}. The line cut of the thermal profile $T_{top}(\mathbf{r},t)$ is also shown. As the goal was to have convection cells over as wide as an area possible for the thermal imaging to yield significant temperature statistics, a large diameter to thickness ratio of the apparatus ($2R/l_z \simeq 225\ mm\ /\ 5\ mm \sim 45$) yielded a stable convection cell pattern $\gtrsim 150$ mm in diameter and stable for as long as the power was applied.

the images. To do this we calculate the Rayleigh Number:

$$Ra = \frac{g\beta}{\nu\alpha}(T_{P_{hot}} - T_{P_{cold}})l_z^3 \tag{8}$$

where g is the acceleration due to gravity and β is thermal expansion coefficient of silicone oil. $T_{P_{hot}}$ and $T_{P_{cold}}$ describe the mean temperature of the copper plate using the thermocouple attached to the base and the IR camera records the mean temperature for the surface of the liquid, respectively. All other values are found either by measuring or in product specifics as seen in Table 1 and Table 2.

The motion of a viscous fluid is described by the Navier-Stokes equations. The solutions to these equations are unsolved mysteries. However, solutions can be approximated using assumptions like incompressible flow and small density variations etc. One such way to solve non-isothermal flow, such as the Rayleigh-Bénard convection without having to solve the Navier stokes is by using the Boussinesq approximation. Under this technique, approximations of an ideal incompressible fluid that is thermally driven can be rewritten by using the following set of equations,

$$\frac{\partial \rho}{\partial t} + \nabla \cdot (\rho \overrightarrow{u}) = 0$$
$$\frac{\partial \overrightarrow{u}}{\partial t} + (\overrightarrow{u} \cdot \nabla)\overrightarrow{u} = -\frac{1}{\rho}\nabla p + \nu \nabla \cdot (\nabla \cdot \overrightarrow{u}) - g\beta\Delta T \tag{9}$$
$$\frac{\partial T}{\partial t} + \overrightarrow{u} \cdot \nabla T = \alpha \nabla^2 T + \frac{\overrightarrow{J}}{\rho c_P}$$

For a packet of fluid with local convective velocity, $\overrightarrow{u}$ incompressibility implies, $\nabla \cdot \overrightarrow{u} = 0$; the density is assumed to vary linearly with temperature, $\rho = \rho_0(1 - \beta\Delta T)$, and the specific heat of the fluid is denoted by c_P.

Rayleigh-Bénard convection, due to its conceptual richness has become one of the most actively studied physical systems. Its dynamics offer extensive insight into both the fluid mechanics and the thermodynamics aspects of natural convection. Over the years, Rayleigh-Bénard convection has especially been used to study the fluid mechanics of turbulent flow while numerous boundary layer studies have been performed to estimate the effect of geometry on convective heat transfer and the role of plumes. One can also find numerous studies on the empirical relationships between the various dimensionless numbers (specially, Nusselt number (Nu), Reynolds number (Re), Prandtl number (Pr) and Rayleigh number (Ra)) under conditions of laminar and turbulent flows [18, 29]. Currently, the fluid mechanics community is interested in solving issues like hydrodynamics, convection cell formation through the role of plumes, rotation and magnetic fields effects on cell placement, turbulent convection with cryogenic gas etc [18, 29, 30, 8, 9]. Although, the current state of the art experimental setups, data logging techniques, numerical and mechanistic simulations have already provided numerous critical insights about the fluid mechanical aspects and more needs to be done in respect to this, a lot of the thermodynamical interpretations still remain unresolved. Our approach does not analyze the system through a fluid mechanics perspective and focuses solely on the thermodynamics behind the images taken through the infrared (IR) camera.

2 Methodology

Rayleigh-Bénard convection is one of the most widely used canonical examples to study pattern formation and since it can be easily recreated, it is also one of the most 'simple' complex systems.

A resistive heat film (heater) is attached to the base of a copper pan. The copper pan has a diameter of 0.225 m and the electric resistance of the heater is $37.5 \pm 0.5\ \Omega$. Copper being a good conductor of heat will allow the flow of energy through it with minimal thermal resistance. Over the copper plate, a thin layer of silicone oil, with a kinematic viscosity of either 10 cSt, 20 cSt or 150 cSt is heated. As seen in Figure 4, the plate is also attached with a J-Type Thermocouple, T_1. The entire experiment is placed within an wooden gasket. The gasket rests on an insulating foam (isolation block) and has an opening on top, from where an IR Camera (FLIR T62101) can image the surface of the plate (as seen in Figure 4). The IR camera is positioned about

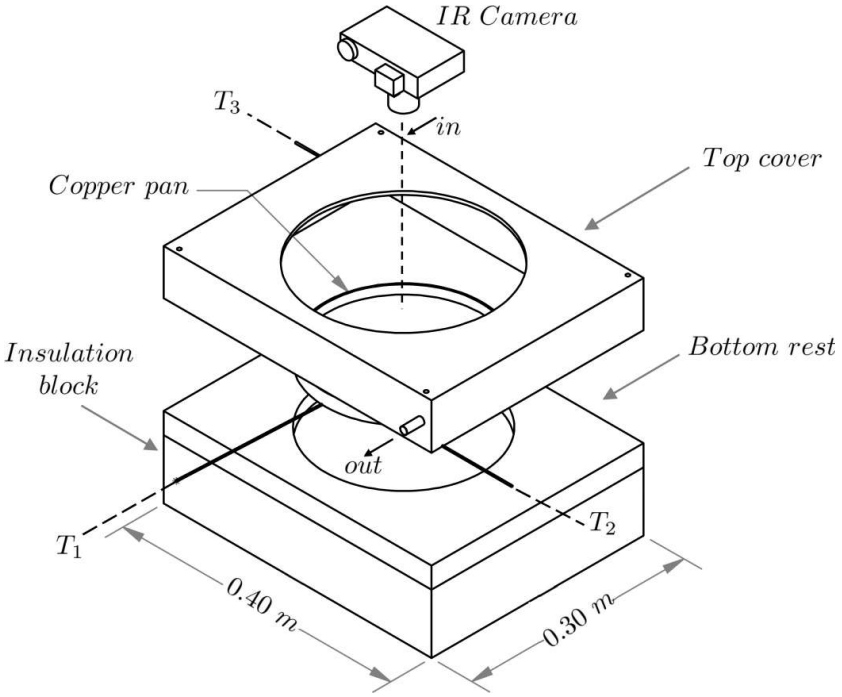

Figure 4: Figure illustrates the experimental setup with the copper pan ($2R = 0.225\ m$), the three thermocouples (T_1, T_2, T_3), inlet and outlet ducts for the forced convective heat transfer, and the Infra Red camera for real-time thermal imaging. The inlet and the outlet ducts are present on the top cover and the copper pan sits on a wooden bottom rest and a polyurethane foam foundation which acts as an insulator.

0.7 m above the plate. The gasket also has two openings allowing for gas exchange, if required for forced convective heat transfer. T_2 and T_3 measure the temperature of the incoming and outgoing gas respectively. The isolation block, which is made out of polyurethane foam, also accounts for the lateral dissipation of heat by fitting right around the copper plate. This sums up the experimental resources needed to create a Bénard Cell.

Since each thermal image has its own temperature scale, a test run with no oil is needed to calibrate the temperature readings of the IR Camera to the temperature readings of thermocouple attached to the base of the Copper plate. This ensures the camera records a similar change in temperature as the thermocouple. In order to do this, adhesive tape is attached to five randomly chosen spots on the surface of the plate and the IR Camera is focused onto the entire plate. Figure 5 represents the calibration curves for these five spots comparing the thermocouple temperature at the base and the IR Camera temperature of the surface. Although it is checked during every run, it can be assumed here on that the IR Camera is now imaging approximately the surface of the liquid that will be placed. This is because the thin layer of Silicone Oil is only about 4 or 5 mm based on the experiment [34].

Data from the thermocouple can be viewed using NI Signal Express while data from the IR Camera can be viewed through the FLIR Software. The FLIR software will allow for remotely accessing the camera and also display statistics for selected regions or points. Any other manual arrangements to the system can be ensured through the real time display as well. All data is structured on a MATLAB Spreadsheet where a fit can be made (Figure 5). The fit will define the amount the camera needs to adjust in order to report a temperature more accurate.

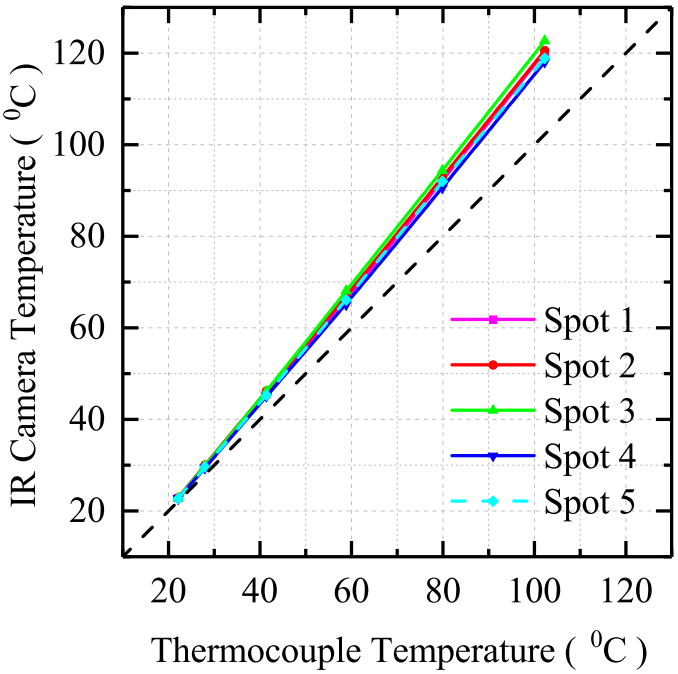

Figure 5: Figure shows the steady state relationship between the IR Camera recorded temperature and the base thermocouple temperature at different power settings for the five randomly chosen spots on the empty copper pan.

2.1 Image Analysis

An IR Camera detects infrared energy (heat) and converts it to bits. This means that every pixel will have an allocated bit value, in this case, between 0 and 255. The bit value determines the intensity of the pixel with 0 being the coldest pixel in the image and 255 being the most intense or 'hottest' in that particular frame or image. The FLIR T62101 has a resolution of 320 x 240 pixels (76800 pixels) with a sensitivity less than 0.045°C at room temperature. However, there is a trade off. The camera does record higher temperatures than it should at higher powers and this is because of the emissivity of the copper plate. We also accounted for this in the calibration curves as seen in Figure 5, but nonetheless the sensitivity fails to be less than 0.045°C. We therefore focus most of the studies for the data below a certain power (usually $95W$-$130W$).

Using the FLIR software, images and videos can be taken and the output can be analyzed or viewed in two different ways. The first would be by taking advantage of FLIR's output matrix and the second would be by uploading the images as a stack in ImageJ. The first approach is more desirable and accurate, however, ImageJ allows for great ways to derive other kinds of statistics like temperature threshold.

Utilizing the FLIR Software, a 2D Array (M x N = 320 x 240 elements) of bit values can be obtained, where every element of the array represents the bit value of a particular pixel. Taking into account the previous calibration of the Camera and the thermocouple, it is now possible to use the scale at the right edge of the image. The scale displays the temperature of the hottest and coldest pixel in °C and assumes a linear conversion from bits to °C. Using the linear equation:

$$y = mx + b, \quad m = \frac{y_2 - y_1}{x_2 - x_1} \tag{10}$$

where 'y' is temperature of pixel in °C and 'x' is the temperature of same pixel in bits. Slope 'm' is determined from the broader range of values with y_2 being the pixel with the highest value in °C and y_1, the pixel with the lowest value in °C. x_2 and x_1 would be the same pixels but the value in bits. The y-intercept 'b' is always taken to be equal to y_1, making it simpler during analysis. This can be rewritten in the form:

$$Temp\,(^{\circ}C) = \frac{Max\ Temp\,(^{\circ}C) - Min\ Temp\,(^{\circ}C)}{255 - 0} \times bit\ \ + Min\ Temp\,(^{\circ}C) \tag{11}$$

Since the camera is not vertically adjusted anymore, the diameter of the copper plate will help convert pixels to meters. The diameter is traced on the image using a software called ImageJ. ImageJ will calculate how many pixels make up a millimeter and output the subsequent results in millimeters. With the following information from the °C matrix, it is now possible to calculate useful statistics.

The second technique mentioned above takes a slightly different approach but could be useful in certain scenarios where plug-ins for threshold calculation in ImageJ may be used. Raw images from the camera can be directly dropped into ImageJ. A feature of ImageJ called Virtual Stack will allow the user to upload more than one image and perform the same operations that will be executed in every image on the same pixel. Since the camera does not move during image collection, it is acceptable for us to be able to use it. Although the approach mentions a different technique it is similar to the earlier one in that the calculations go through the same procedure and we assume a linear conversion from bits to °C. A region is selected using the oval selection tool. The region's mean, standard deviation and other statistics can be obtained through 'set measurements'. With this technique however the mean temperature corresponds to the temperature of the the surface of the oil, T_{top}. T_{bottom} remains as the temperature readings from the thermocouple attached to the bottom of the copper plate [34].

2.2 Outline

Now that we have data that shows the intensity of the image (i.e. the $M \times N$ matrix in $^{\circ}C$), we can use this to calculate statistics like mean temperature and standard deviation for every image. We then expand the technique with the infrared camera to map the convective instability of the surface of the liquid across different external powers as seen in the sample snapshots in Figure 6[a]. All the while we make sure that the applied power never exceeds a value that can change the molecular configuration of the oil through burning or extend the system into the turbulent regime by boiling. This means that the Rayleigh Number (Ra) <3500. We can now use this data to understand how the system behaves in space.

At each power we also take time lapses (or a series of images usually about 480 to 900 images) for the liquid beginning at room temperature steady state and ending when the system reaches a position where the thermal fluctuations are less than $1/10^{th}$ of a $^{\circ}C$ (this usually takes about

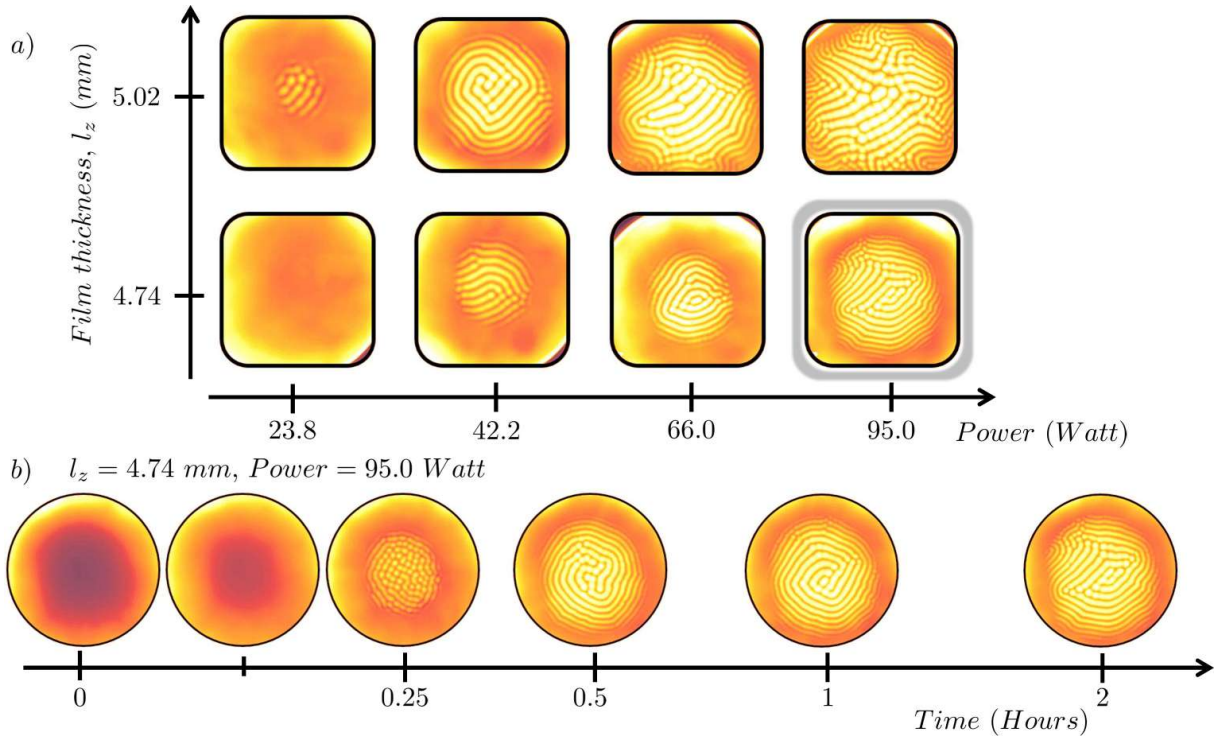

Figure 6: a) Figure shows steady–state thermal images recorded for two thickness, lz = 4.74 mm and 5.02 mm at various powers. b) Figure shows the time–evolution of the lz = 4.74 mm at 95.0 W over a period of two hours. Note that the shown images are logarithmically placed in time.

2-3 hours) as seen in the sample snapshots in Figure 6[b]. This data is used to understand how the system behaves in time.

3 Manufacturing of Setup

The initial setup had some fundamental limits to it. For example, the thickness of the walls were only 0.8cm high and this forced us to play with lower thicknesses of the liquid which was perfect for non-turbulent studies but not for turbulent conditions in which we needed a higher thickness. Another problem we faced was the flatness of the copper plate. Due to the manufacturing process of the initial setup we faced difficulties in trying to manage the uniform distribution of the patterns across the surface of the liquid. However, for our initial experiments these issues were not dominant as the thickness of the liquid was thin enough. As a part of this MQP, we also created a new setup to avoid future issues like this.

To be able to avoid the earlier issues we needed to change the way we manufactured this setup. Instead of a press style approach in which a single sheet of copper was pressed and the sides were bent normal to the sheet, we decided on a clamped style approach. A thin square sheet of copper was placed between two square blocks of aluminum and together the three layers had six tapped holes (through all) around a circumference of 24 cm from the center as seen in Figure 15. A circular hole on the aluminium block at the top was machined all the way through. The hole had a diameter of 22.5 cm. This was our approach to recreate the previous setup but with a flatter copper platform and higher walls around (aluminum block on top). The entire

setup was manufactured in Higgins Laboratories with the help of the VM2 mill while ESPRIT files executed the instructions. The design was also adapted to make space for the heater that was attached to the bottom of the copper plate and a small hole allowed for the thermocouple and wiring's to the heater to fit through. In order to fully make sure that the liquid did not seep through gaps between the copper sheet and aluminum block placed over it, we also used high temperature silicone sealant that acted like an adhesive between the block and the copper sheet.

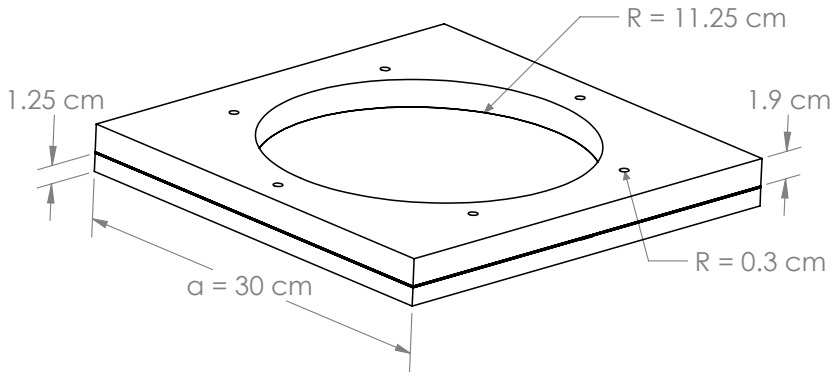

Figure 7: Figure illustrates the manufacturing setup with the copper sheet bolted between two aluminum blocks. The aluminum block on top is machined to include a hole ($2R = 0.225\ m$) in order to directly see the copper sheet underneath and six tapped holes allow for the bolts to fasten. The Aluminum block on top also acts like the boundary (walls) for the liquid poured over the copper sheet.

After initial trials that confirmed that the setup worked, the entire structure replaced the copper plate in Figure 4 of the previous setup. The setup had finally enabled us to perform experiments with higher thicknesses and moreover allowed us to use a near flat copper base. CAD and CAM files are included in this MQP.

4 Results and Discussion

This methodology helps us quantify spatio-temporal thermal fluctuations in a driven out-of-equilibrium steady state system like the Rayleigh-Bénard convection. As mentioned earlier each of the images are converted to M×N matrices with temperature in $^{\circ}C$ and statistical analysis can now be performed by choosing a region of interest (ROI). The ROI depends based on what the focus is but it can be square, a circle, area between two concentric circles or list of pixels with temperature above a threshold. A square is selected by defining the coordinates of upper left corner (x_1, y_1) and the bottom right corner (x_2, y_2), i.e. the diagonal points. Similarly a circular or annular region can be extracted by specifying the center point and the radii (inner and outer circle) of the respective circles. Isolating regions of interest allows for calculating statistics and can enable us to chart down how the different viscosities or thicknesses or powers affect the temperature distribution on the surface of the liquid. Table 1 highlights the properties of silicone oil at 150 cSt.

Table 1: Table outlines thermal and material properties of the silicone oil sample that was used to perform the current study [**?**].

Viscosity ν (cSt)	*Density* ρ (Kg/m^3)	*Conductivity* k $(W/m-K)$	*Specific Heat* $c_{p_{oil}}$ $(J/Kg-K)$	*Diffusivity* α (m^2/s)	*Compressibility* β_T (m^2/N)
150	970	0.16	1500	1.099×10^{-7}	9.5×10^{-4}

Table 2: Table shows the calorimetric data from the steady–state images at different powers for the two thickness ($l_z = 4.74\ mm$ and $5.02\ mm$). The numbers listed in the first column denote the specified points in the plots shown in Figure 10. The top temperature (T_{top}) is recorded by the thermal camera, bottom temperature (T_{bottom}) by the thermocouple T_2, the hot and cold spot temperatures ($T_{P_{hot}}$ and $T_{P_{cold}}$) are obtained by spatially averaging regions of interest (P_{hot} and P_{cold}) from the thermal images, conduction temperature (T_{cond}) is calculated from Equation 11, and the Rayleigh Number ($Ra = \frac{g\beta l_z^3}{\nu\alpha}(T_{bottom} - T_{top})$) from the listed values in Table 1.

l_z (mm)	#	*Power* (W)	T_{top} $(^\circ C)$	$T_{P_{hot}}$ $(^\circ C)$	$T_{P_{cold}}$ $(^\circ C)$	T_{bottom} $(^\circ C)$	T_{cond} $(^\circ C)$	*Rayleigh Number* Ra
4.74	1	23.8	39.4	$--$	$--$	53.2	46.8	831
	2	42.2	48.4	61.5	54.8	71.7	61.7	1410
	3	66	59.9	78.2	69.7	89.5	76.1	1790
	4	95	70.9	100.9	91.1	115	96.4	2670
	5	130	89.8	124.8	114.1	147	122.2	3464
5.02	1	10.5	30.3	$--$	$--$	37.9	34.5	535
	2	23.8	38.1	43.1	39.7	53.4	46.9	1080
	3	42.2	47.2	63.5	56.7	70.9	60.9	1670
	4	66	58.8	84.4	73.6	91.8	77.7	2330
	5	95	73.1	101.3	90.1	115	96.4	2960

Table 2 highlights the data gathered and extrapolated from the matrices in $^\circ C$. Two main thicknesses that were played around with are $l_z = 4.74\ mm$ and $5.02\ mm$. The power supplied was incrementally increased and the steady state non-equilibrium images were used to highlight the last temperature recordings for each power (Table 2). T_{cond} and Rayleigh Numbers were calculated as seen later on in temperature plots.

As mentioned earlier the data comes from spatially averaging the statistics on regions of interest. In Figure 8, the analysis strategy is pictorially represented to give a better idea of how we account for space and time. Figure 5[a] represents how a specific region is followed across in time to extract temporal statistics whereas in Figure 5[b], a region of interest is looked at across the steady state image (final image) in order to extract spatial statistics. In Figure 5[b] the region R denotes the section of the image that does not display convective patterns and the region P is where the patterns are visible.

4.1 Spatial Results

Spatial statistics are taken from the final image in the time lapse. The last image is at non-equilibrium steady state. This means that the image was taken when the thermal fluctuations are less than than $1/10^{th}$ of a $^\circ C$. The image was usually seen across different powers after slightly more than 2 hours of observation.

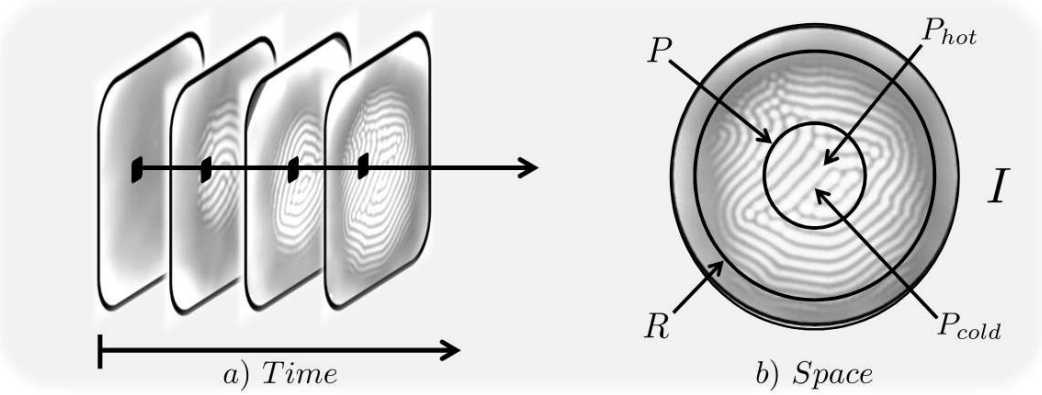

Figure 8: a) Figure illustrates the temporal analysis of an arbitrary region of interest on the images as a function time as the system evolves from room temperature equilibrium to an out–of–equilibrium steady–state. b) Figure shows the regions of interest for the spatial analysis on the steady–state image of a Rayleigh–Bénard convection. The complete image is denoted by I, the annular region without any structures by R, the circle at the center by P, the upward (bright spots) and downward plumes (dark spots) by P_{hot} and P_{cold} respectively [5, 34]

4.1.1 Distributions

The first study performed was to see how the thermal profile looked in regions with patterns (i.e. convection), P, and compare them to regions where the patterns were not visible, R in Figure 8[b]. Because convection can be seen clearly over the images, it was easy to isolate the two and define circular or annular regions of interest on the images. Every pixel with its corresponding temperature, T_{ij}, within the region of interest is stored in a 1D array and a frequency histogram is generated to model the distribution of temperature across space. A measure, μ is defined over the collection of all pixel temperatures within a region (P or R) such that,

$$\delta T^* = \frac{1}{\mu(P)} \int_{\mu} \delta T^*(P) \tag{12}$$

In Figure 9, the left panel (a and c) shows the histograms and the kernel density approximations for the region of interest with convection (in green on the images) for the two thicknesses. As one can see there is a clear bi-modality and this suggests that the ergodicity of the system is broken and moreover, broken spatially [15, 23]. However, like in the middle panel (b and d) the outer regions of interest with no convection (between the red circles on the images) shows a histogram that can be fit with a near perfect cumulative Gaussian distribution function. This suggests that thermal fluctuations in this region are purely random (normal distribution) while those within the convective boundary also contain gradients along with the fluctuations, and, together they contribute to the temperature spatial variance [22].

If we look closer at the bi-modal distributions, it can be identified clearly that there are two different peaks here. So we performed two independent Gaussian fits over the data. This was done by selecting a threshold that allowed for all colder pixels within the ROI to be below the threshold and all the hotter pixels within the ROI to be above the threshold. The temperature data was split into two different arrays by this process and the respective histograms were created. ImageJ was a useful factor in retrieving the threshold information here. This is illustrated in

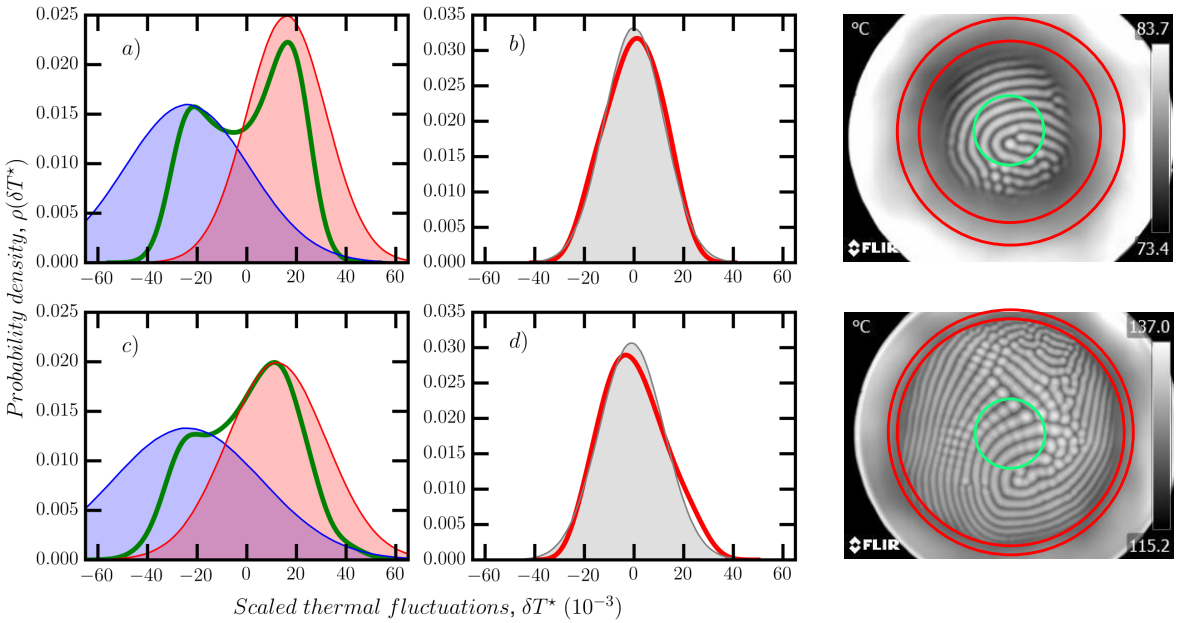

Figure 9: Figure shows the scaled-thermal fluctuations in a Rayleigh-Bénard convection under steady-state at 40 Volt (top panel) and 60 Volt (bottom panel) at Ra=3464. The probability density plots on the left ((a) and c)) captures the fluctuations in the annular region (in cyan) with Gaussian fits (light gray, shaded) centered at the origin, while the plots on the right ((b) and d)) captures the fluctuations in the closed circular region (in red).

Figure 10.

The two independent Gaussian fits are performed and denoted by $\mathcal{N}(\mu_k, \sigma_k^2)$ where μ_k and σ_k^2 represent the mean and variance respectively. For example in Figure 10, $\mathcal{N}(89.25 \pm 0.089, 1.25)$ accounts for the hot region (in red) and $\mathcal{N}(86.21 \pm 0.13, 1.24)$ accounts for the cold region (in blue). As you can see the histograms are normally distributed in Figure 10c and 10d. Figure 10c represents the histogram with $\mathcal{N}(89.48\pm, 0.64)$ for the hot region and Figure 10d represents the histogram with $\mathcal{N}(86.49\pm, 0.96)$ for the cold region.

4.1.2 Temperature Plots

From the tabulated data in Table 2, it is possible to now understand how temperature changes across the surface with change in applied power. Moreover, it has also enabled us to understand how convection plays a role in here. If there was to be no convection then temperature across the surface of the liquid will be characterized by the dominant form of heat transfer, conduction. We can calculate this theoretical conductive temperature, T_{cond} using the steady state heat conduction equation and the available calorimetric data in Table 1. Compressing and rewriting all this in one line, we will get:

$$\dot{Q} = \frac{(m_{Cu}c_{p_{Cu}} + m_{oil}c_{p_{oil}})(T_{bottom} - T_{top})}{2 \times 60 \times 60} = -kA\nabla T = -kA\Big(\frac{T_{cond} - T_{bottom}}{l_z}\Big) \tag{13}$$

where A is the area of the copper pan, l_z is the thickness of the fluid, Table 1 shows the expected temperature of theoretical conductive layer, T_{cond} which is measured and like previously

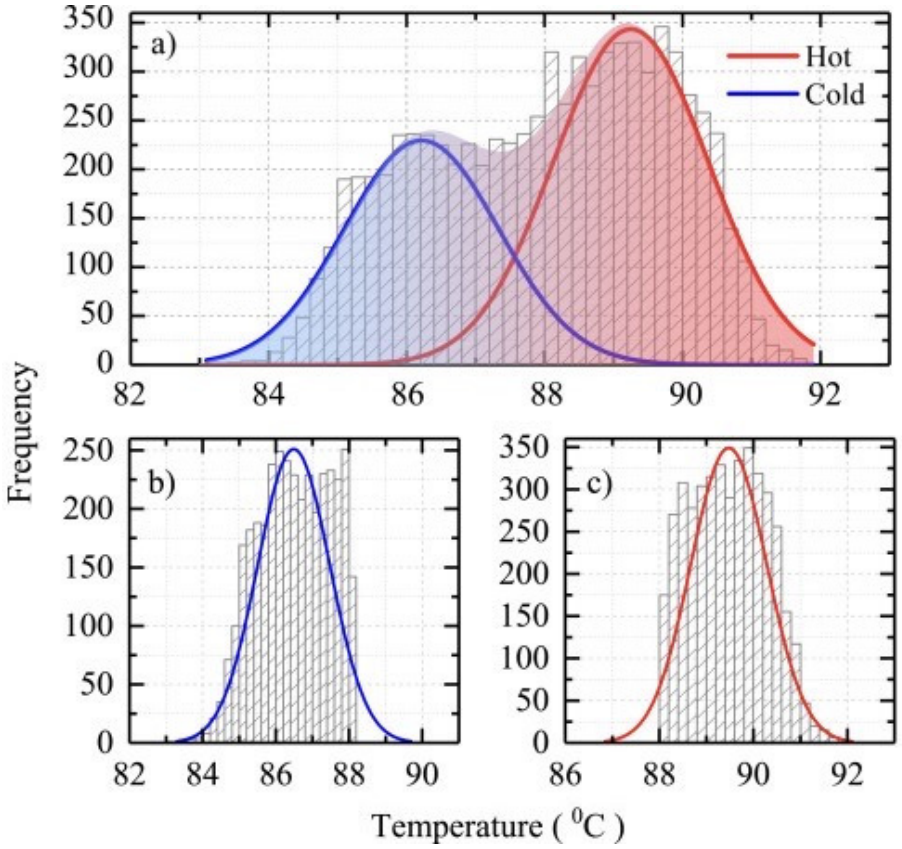

Figure 10: Figure a) shows a bimodal distribution of the temperature frequency distribution in the ROI with the pattern. Two independent Gaussian distributions (b and c) are performed which are identified as 'hot'(in red) and 'cold'(in blue) to the left and right.

mentioned the temperature of the upward and downward plumes are ($T_{P_{hot}}$ and $T_{P_{cold}}$). It is also observed clearly that, $T_{bottom} > T_{conduction} > T_{top}$, across the entire spectrum.

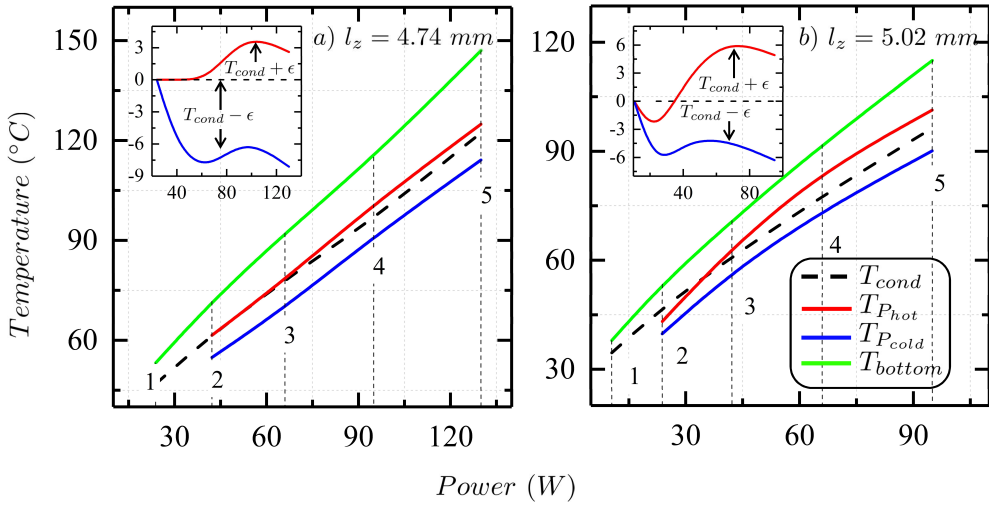

Figure 11: Figure shows the temperature plots ($T_{P_{hot}}, T_{P_{cold}}, T_{cond}$ and T_{bottom}) for the steady-state images at different values of input power for a) $l_z = 4.74\ mm$ and b) $l_z = 5.02\ mm$. The inset plots capture the variation in the plume temperatures ($T_{P_{hot}}$ and $T_{P_{cold}}$) about the theoretical conduction temperature (T_{cond}) as a function of power. For details about the specific points denoted in the plots, refer Table 2. Also, note that ϵ is arbitrary.

In Figure 10, we plotted the temperatures of the calculated values of T_{cond} along with the

measured values of $T_{P_{hot}}$ and $T_{P_{cold}}$ as function of the power supplied to the pan. Whenever the Rayleigh Number was higher than 1708 we did see convection and the theoretical conductive temperature was close to the weighted average of the temperature of the hot and cold plumes [9].

We also show the variance of these plume temperatures as a function of the power applied in the inset of Figure 11. ϵ tells us how much change their can be above and below the T_{cond} trend-line. It is arbitrary because we don't really know what the actual value is. Although it confirms our understanding that the theoretical conductive temperature should be between the hot and cold plume temperatures, it was informative in the sense that we can see that this is not a linear relationship. The variation grew on opposite sides of the T_{cond} "almost anti-symmetrically" [5]. In conclusion, the data suggests a sort of spatially varying character to this system and the spatial analysis corresponding to $T_{P_{hot}}$ and $T_{P_{cold}}$ can be thought of as two different local equilibrium like regions that coexist with each other [17]. As documented earlier this is one of the ways we can begin to understand how non-equilibrium systems behave using the local equilibrium hypothesis [31].

4.1.3 Precursor to Length Scales

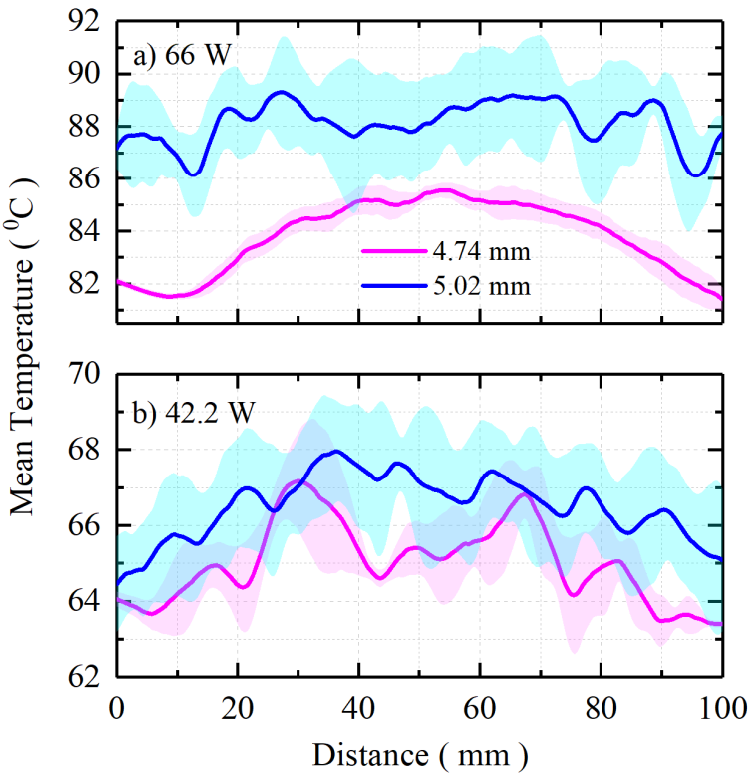

Figure 12: a) Figure shows the mean thermal profiles of six spatially averaged horizontal lines for $L_z = 5.02$ (blue) and 4.74 mm (magenta) at 66W. (b) Figure shows the mean thermal profiles of six spatially averaged horizontal lines for $L_z = 5.02$ (blue) and 4.74 mm (magenta) at 42.2 W. The shaded bands about the mean thermal profiles represent the standard deviation.

An important technique to analyze how the pattern's length scales develop can be done by using auto-correlation techniques, specifically the Wiener–Khinchin theorem. However, a more easy and quick way to see if there are length scales within the system is by simply checking

mean temperature across a line of pixels. Before we used the auto-correlation equations to do this, we plotted the thermal profiles that are spatially averaged along six horizontal line cuts that arranged to be parallel with each other.

As one can see mean temperature for a higher powers (Figure 12[a] - 66W) is greater than those with lower powers (Figure 12[b] - 42.2W). The variation in strength of the thermal profiles describe the thermal field heterogeneity. The more flat a curve is, the easier it is to identify spatial correlation length scales and that's why at higher powers (66W) it can be observed that the temperature was more uniform over longer length scales than for those at lower powers (42.2W). However, this could also be the case that the temperature profiles are not fully developed at lower powers, making the patterns randomly oriented. Since the patterns occupy a smaller area, the majority of the peripheral region experiences mostly conduction and this may also lead to more thermal heterogeneity. This tells us that as the power increases the patterns become more developed and homogeneous. The patterns are chaotic and most of all uneven and in order to construct a more detailed geometry of the region spatially we need to integrate over the whole area which is where we use the Wiener–Khinchin theorem.

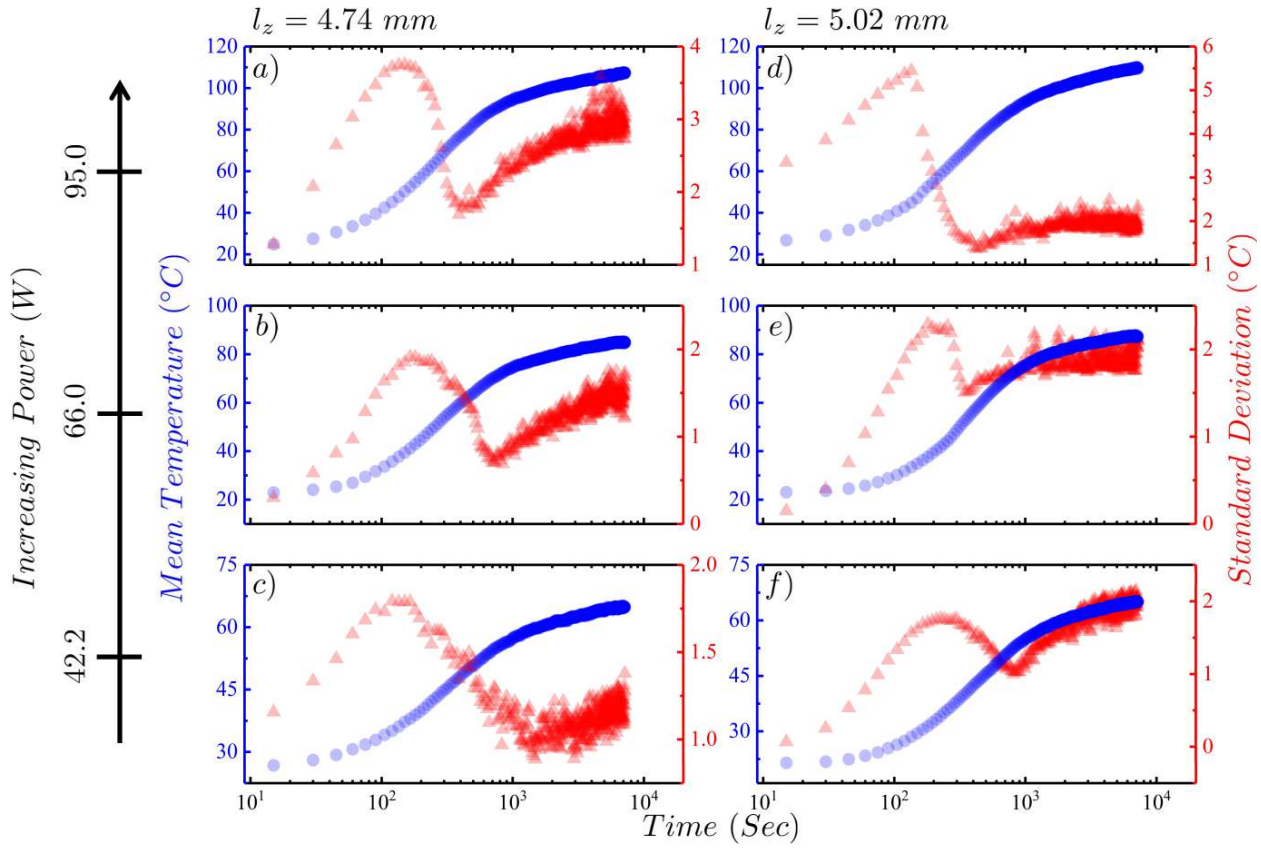

Figure 13: Figure shows on a semi-log scale the temperature mean and standard deviation as a function of time of the top of the silicone oil film as it responds to the applied heating power until steady-state is reached for various values of input power. The left axis corresponds to the temperature mean in degrees Celsius (solid blue circles) and the right axis corresponds to the standard deviation (solid red triangles). Plots a, c, e show heating profiles for a film thickness of $l_z = 4.74\ mm$, and plots b, d, f for $l_z = 5.02\ mm$. Note that the applied heating power in Watts are labeled by the far left $y-$axis.

4.2 Temporal Results

Unlike spatial analysis, time statistics are taken from a time lapse. The time lapse begins just before the a power is supplied to the pan (room temperature equilibrium) and the last image is taken when the system reaches a far-from-equilibrium steady state as seen in Figure 6[b]. The Flir Camera's time lapse feature enables us to take images every 15 seconds and since it takes almost two hours to reach a position where the thermal fluctuations are less that $1/10^{th}$ of a $^{\circ}C$ we get around 481 images.

4.2.1 Temperature Plots

A natural reaction to this data set is to see how the mean temperature and the standard deviation of the surface of the silicone oil evolve as a function of time. A region of interest is selected (a circle encompassing the boundary of the plate) and we then average all the pixels with in it using our computational image analysis technique.

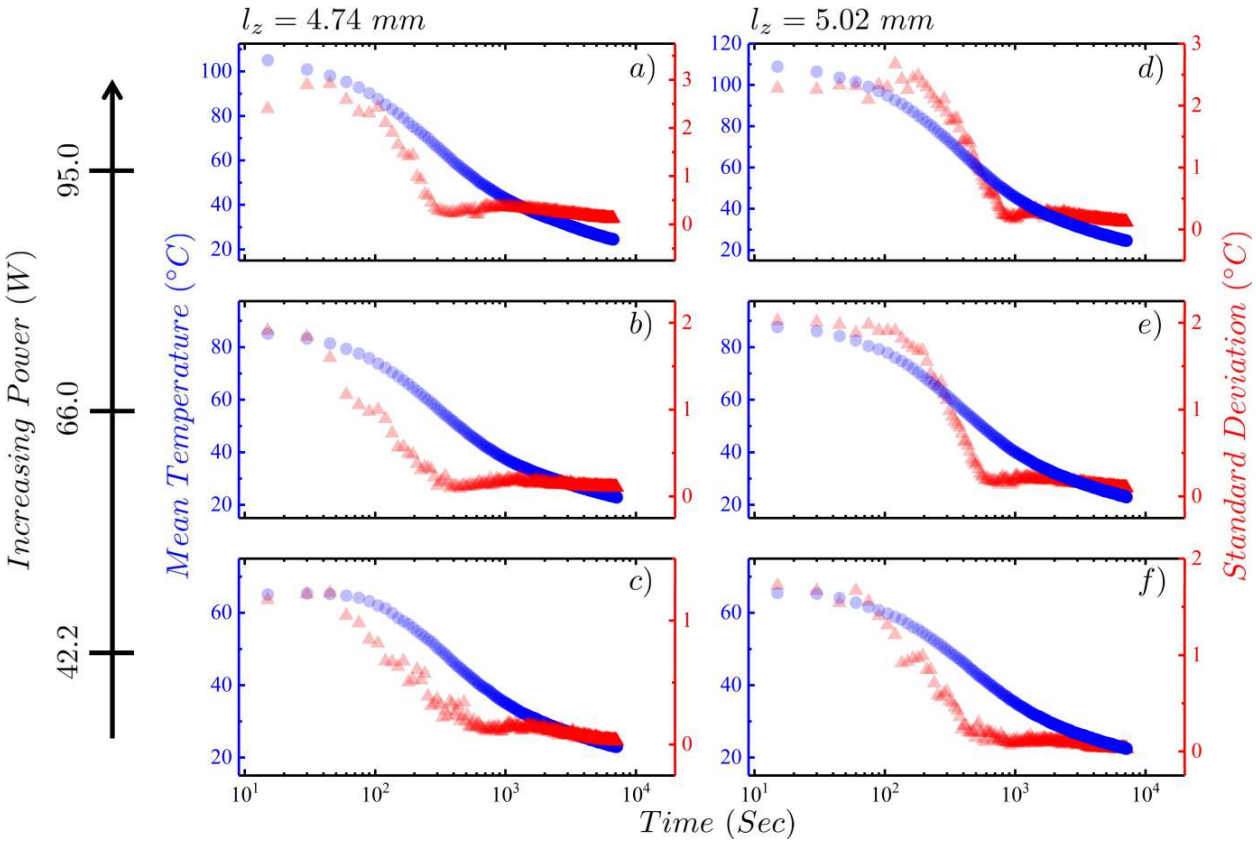

Figure 14: Figure shows on a semi-log scale the temperature mean and standard deviation as a function of time of the top surface of the silicone oil film as it relaxes to room temperature after the applied heating power is removed. The left axis corresponds to the temperature mean in degrees Celsius (solid blue circles) and the right axis corresponds to the standard deviation (solid red triangles). Plots a, c, e show cooling profiles for the film thickness of $l_z = 4.74\ mm$, and plots b, d, f for $l_z = 5.02\ mm$. Note that the applied heating power in Watts are labeled by the far left $y-$axis.

Figure 8[a] highlights the approach we use to track the region across images. The mean temperature of the region of interest is $\langle T \rangle = \frac{1}{N} \sum_{i,j \in I} T_{ij}$ and the standard deviation, $\sigma_T =$

$\sqrt{\frac{\sum_{i,j\in I}(T_{ij}-\langle T\rangle)^2}{N-1}}$, and they are both calculated from the image matrix (I_{ij}). The same region of interest is used across all the images and the data is graphed as seen in Figure 13.

An interesting result from this was the unexpected drop in standard deviation as the patterns began to form around ≈200 seconds into the process. Standard deviation measures the thermal fluctuations in the system and this suggests that the increasing trend of thermal fluctuations is broken at the onset of convection. At around ≈900 seconds this value reaches a minimum and begins to increase till the mean temperature stabilizes. During this period convection cells grow to their maximum extent over the film. Note also that the maximum mean temperature at steady state for the sample increases with an increase of power supplied.

We then recorded this entire process as the system begins to cool when the power supplied to the system is turned off as seen in Figure 14. Unlike when the power is turned on, this time the mean and standard deviation fall abruptly until the cell patterns disappear. The fall in standard deviation begins to slow down when the patterns disappear and flattens as the mean temperature reaches room temperature. It is again seen through the whole temperature plots that standard deviation is dominated by these spatial thermal fluctuations so long as there is no convection. But as soon as convection cells appear, thermal gradients across the film affect the standard deviation and there is this "unexpected and sudden" change [5].

4.2.2 Distributions

This next section of the temporal plots account for the region changes after it has reached steady state. We know that fluctuations decay when a system is at equilibrium state as a function of $1/\sqrt{N}$ and this is also the case for fluctuations at far-from-equilibrium steady state when it is considered independent of time and space (equivalence principle in thermodynamics)[1]. Therefore we can say that after the system has reached steady state and we will get normally distributed histograms. This section shows that.

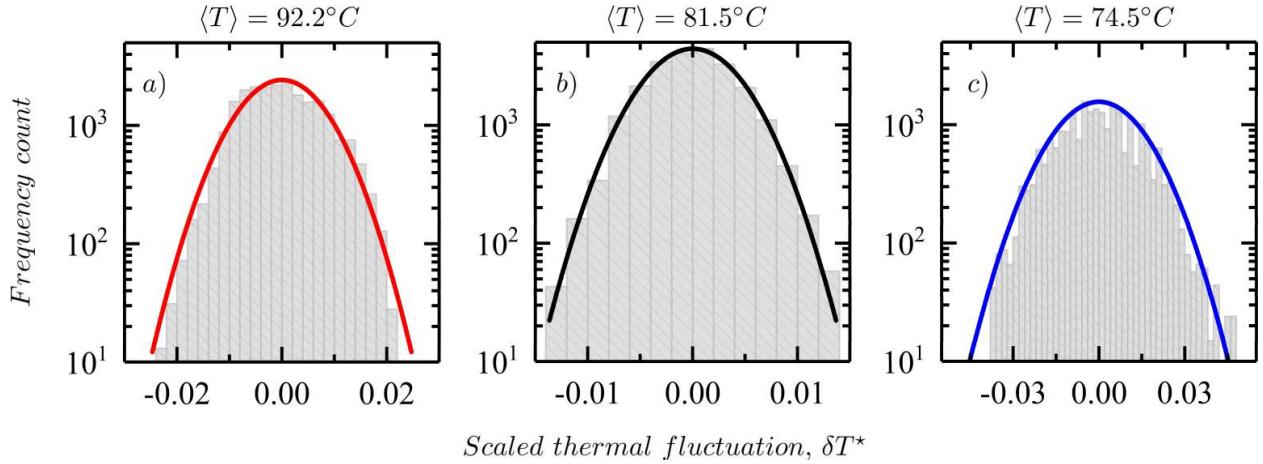

Figure 15: Figure shows the histograms for the scaled-thermal fluctuations averaged over time after the system has reached a steady-state on a semi-logarithmic scale. The panels a) denote the hot regions (P_{hot}), b) the entire region (P), and c) the cold regions (P_{cold}). The mean temperature, $\langle T\rangle$ (in $^\circ C$) of the various regions of interest are also denoted. The histograms are fitted with normal distribution functions all centered at zero.

To do this we take a video (a movie) at 30 frames/sec for 15 minutes. The region of interest which is fixed across the whole movie is extracted. This region is either one that has no patterns within it or one over a hot or cold plume (part of a convection cell). This can be seen in Figure 15, that shows the time-averaged scaled thermal fluctuations over these particular regions. Thermal fluctuations are calculated by finding the difference between the global mean and every pixel temperature within the ROI. This is then scaled using that same mean by $\delta T^\star = \frac{T_{ij} - \langle T \rangle}{\langle T \rangle}$. Averaging across all frames (which is about 27000 frames) for the entire video, the $\delta T^\star$ then becomes:

$$\delta T^\star = \frac{1}{T} \int_0^T \delta T^\star(t) dt. \tag{14}$$

As seen in Figure 14, we accounted for different regions of interest and saw that they are all normally distributed. Figure 14[a] and 14[b] show the time averaged histograms for the hot and cold plumes and Figure 14[b] is for a entire region with patterns, P (seen in Figure 7[b]). The plots were on a semi log y axis to highlight the deviations from the fit near the tails. This can be seen especially on the distributions of the cold plumes in Figure 14[b] suggesting the presence of higher time scales or moments. The combined distribution does not reveal the deviations near the tails from the normal because the distribution is dominated by the hot plumes. Moreover to understand how distribution works in respect to time scales we will need to do auto-correlation using the Wiener–Khinchin theorem again but this time, averaging over every image in the time series.

5 Future Work

Due to the nature of the experiments and its features that can be recognized across other far-from-equilibrium systems, the studies can be extended to incorporate various other phenomena. Although there wasn't enough time to do all of this, we did begin some and also designed further experiments. Here are a few:

5.1 Turbulent Rayleigh-Bénard Convection

A natural extension to the main study of non-turbulent Rayleigh-Bénard Convection is to look at how the statistics change when turbulence arises using the same methodology. Turbulence is achieved at higher Rayleigh Numbers and we attempted to recreate the system for this case by using glycerol-water mixtures [24]. Glycerol-water mixtures are the best liquids we could use for this because they are not only cheap but also allow for a wider range of Rayleigh Numbers that can be played around with (different concentrations of glycerol and water). The new setup also allowed for higher thicknesses which is required for turbulence.

Figure 16 plots the scaled standard deviation of the intrinsic value and order as a function of time (temporal results) for the Rayleigh-Bénard Convection system. The intrinsic value is the spatially averaged temperature, $\langle T(t) \rangle$ and this is denoted by $\langle T(\infty) \rangle$ at steady state. Figure

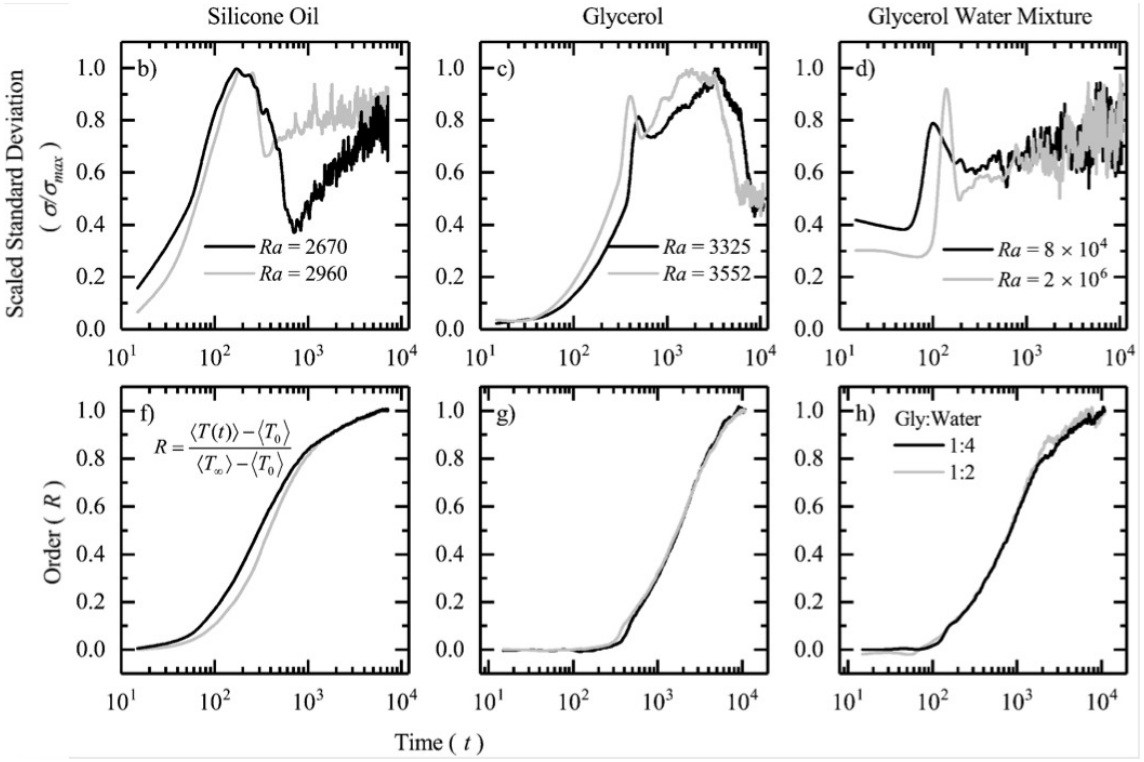

Figure 16: Figure shows the scaled standard deviation of the temperature and the evolution of the order parameter as a function of time (log-scale) for different fluid samples. Note that the Rayleigh Number changes from non-turbulent to turbulent.

16[b] and 16[f] are the graphs we saw earlier for the silicone oil experiments which show non-turbulent Rayleigh-Bénard Convection. The same experiment was performed using glycerol which at the same conditions does not push the system into turbulence (Figure 16[c] and 16[g]), however when mixed with water at 1:4 or 1:2 ratios by volume, achieve Rayleigh Numbers high enough to be turbulent (Figure 16[d] and 16[h]) [4].

The drop in standard deviation across both turbulent and non-turbulent regimes connects them. The dissimilarities like the presence of multiple peaks and unusual drops suggest that there exists various time scales. Overall, these results correlate the spatial ordering of the convective cells with the evolution of the systems temperature manifold. Space and time do not work symmetrically and therefore these systems, both turbulent and non-turbulent are non ergodic [10].

Future work on this can delve into other features of the turbulent Rayleigh-Bénard Convection and assist in making a better comparison to non-turbulent regimes. Statistics across space and time can show how different turbulence can get even though there is a common feature of the spontaneous reduction in local entropy. However this was the extent to which we could finish in this setting.

5.2 Complex Network Framework

This particular study deals with the idea that the 2D matrices (images) from the FLIR Camera which highlight convection patterns can be modeled by complex networks in order to

evaluate the various statistical properties that emerge [3]. The framework will help us understand the patterns and the matrices from a mathematical sense. This could eventually help us connect the current energy studies on Far-from-equilibrium systems to Network theory. However this is a work in progress and although preliminary studies have already been conducted the analysis and logic is still in the early stages of development.

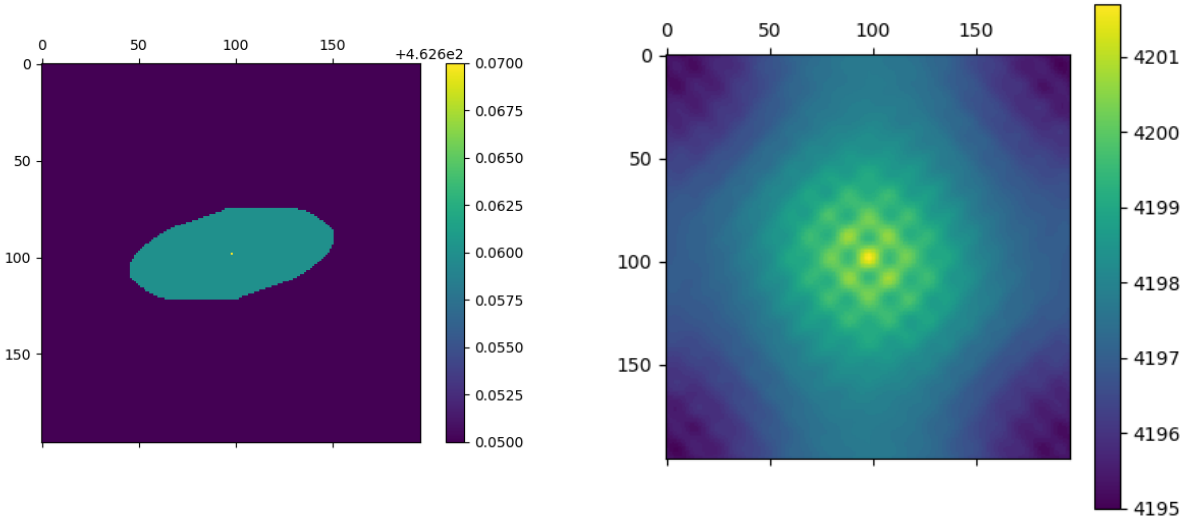

Figure 17: A heat map of the after effects of the application of the autocorrelation function. Figure 17 [a] (left) is the room temperature image and the Figure 17 [b] (right) is the steady state image for a non-turbulent 40V data set.

One of the tools we use for this is called the autocorrelation function. An autocorrelation function is a measure of how similar or dissimilar values are with respect to the values around them. The range is described by values from 0 to 1, where 0 says the value has no correlation and 1 means that it is perfectly correlated or is the same value. Usually an autocorrelation function begins at the point of origin or in this case the center of the matrix (from the Rayleigh-Bénard Convection) and moves radially outward. The simplest and most traditional way to calculate the autocorrelation function is by using the Wiener-Khinchin theorem. The Wiener-Khinchin theorem calculates the autocorrelation through a relation of the functions' spectral density (which is to say that it uses the Fast Fourier transform) and the complex conjugate of the spectral density. It is written in the form:

$$\mathcal{G}(m) = \int_{-\infty}^{\infty} \hat{f}(m)\bar{\hat{f}}(m)e^{i2\pi xm}dm \tag{15}$$

where $\hat{f}$ is the Fourier transform of f and $\bar{\hat{f}}$ is the complex conjugate of the Fourier transform of f [32]. When the autocorrelation function is applied across a 2D matrix from the Rayleigh-Bénard Convection images, we get another 2D matrix with all diagonal values equal to 1 because they are perfectly correlated with themselves while values on either side of the diagonal are equal

and have opposite signs because they represent the correlation of a pixel A with pixel B and pixel B with pixel A. We neglect the diagonal elements by setting them equal to 0 and then take the absolute value of the whole matrix, which is now consisted of values between 0 and 1 (instead of -1 to 1). This logic can be seen in the python supplement,"Autocorrelation.py".

However, in order to build a network model, we need values to be either 1 or 0 and nothing in between. A value of 1 suggests that there is a link connecting a pair of nodes while 0 says there is no link. From trial and error, a certain threshold (T) can be considered to change all values greater than T to 1 and all values less than T to 0. While this is a simplified approach, in reality a stochastic model is used to predict this threshold. Future work would need to incorporate this.

The networkx library in python takes this matrix filled with 1's and 0's and converts it to a MultiGraph component (group of nodes connected indirectly) by changing the 1's into nodes and allocating edges across these nodes. In our case the edges are undirected and the network is a giant component meaning that any node is reachable from any other (this is used because we know fluctations arise randomly). A networks framework allows us to calculate path length, avg degree distribution and many more insights into topological features of the layout.

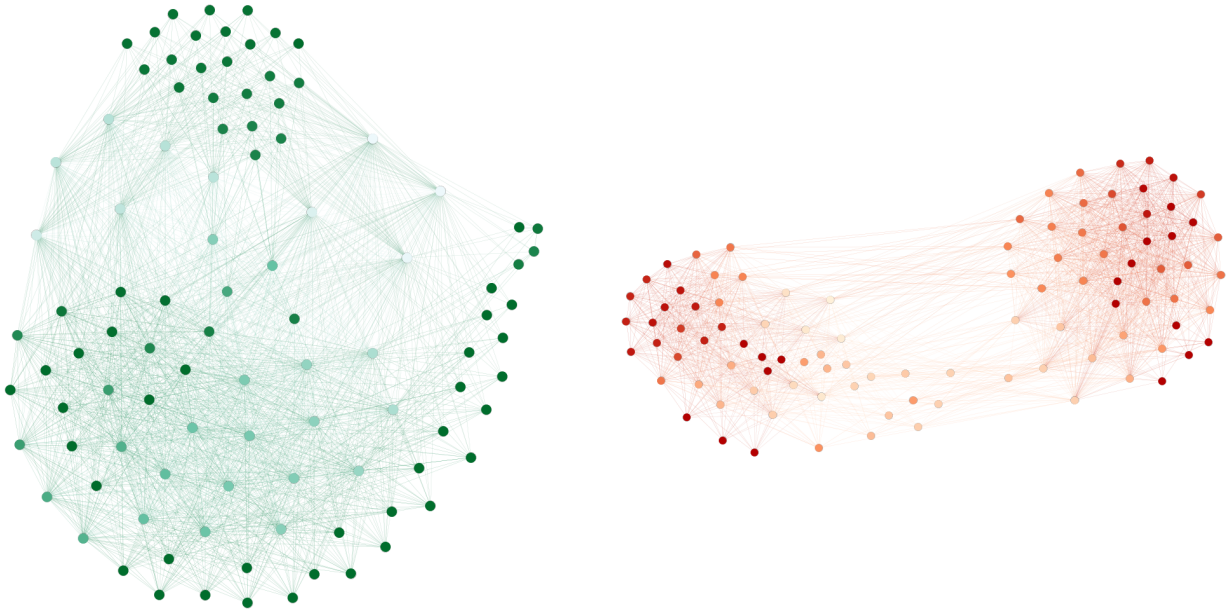

(a) Room Temperature Image

(b) Steady State Image

Figure 18: Gephi Visualization of the respective networks for the 40 V non-turbulent dataset.

For this particular study of the 40V room temperature image and its steady state counter part, we were able to see that the number of edges is greater for the room temperature image (2310:1754). Naturally, this should be the case because we know that most pixel temperatures are identical in room temperature matrices. However to fully understand this, we would need to perform a time series analysis to see how the number of edges fall before they begin rise as patterns form. Another interesting feature is the network's average path length which represents the average distance between any two nodes. As expected this increases from 1.54 for the 40V room temperature image to 1.9 for the steady state image. An increase in path length measures the efficiency of the transport phenomena and therefore we know that network has become

more efficient as patterns form. Notice how in Figure 18[b], there are two distinct regions in the steady state image, the segments account for the hot and cold spots respectively. Other information regarding the degree distribution or number of connections in a network is also used to understand structural and dynamical features of the network. However, this is the extent to which the MQP has dealt with. Future work would look into how to connect all this together and figure out if the Rayleigh-Bénard Convection system can be modelled accurately through complex networks. Codes are attached to this MQP.

5.3 Precursor to Information Theory

Throughout the study we have looked at how energy plays a vital role in the emergence of order and how the statistics change as a result. However, there is a completely different way to look at these studies altogether and it is by using information theory. The Rayleigh-Bénard Convection can be thought of a system that sends and receives information in order to maintain its own stored data. Moreover, the theory inherently brings the idea of entropy into the picture. In information theory, entropy quantifies the amount of uncertainty in the outcome of a random process [27]. Before we delve into such a topic, we tried to first replicate the system mathematically. That is to say, how would you make up the Rayleigh-Bénard Convection if you did not have an IR Camera to image the surface of the liquid.

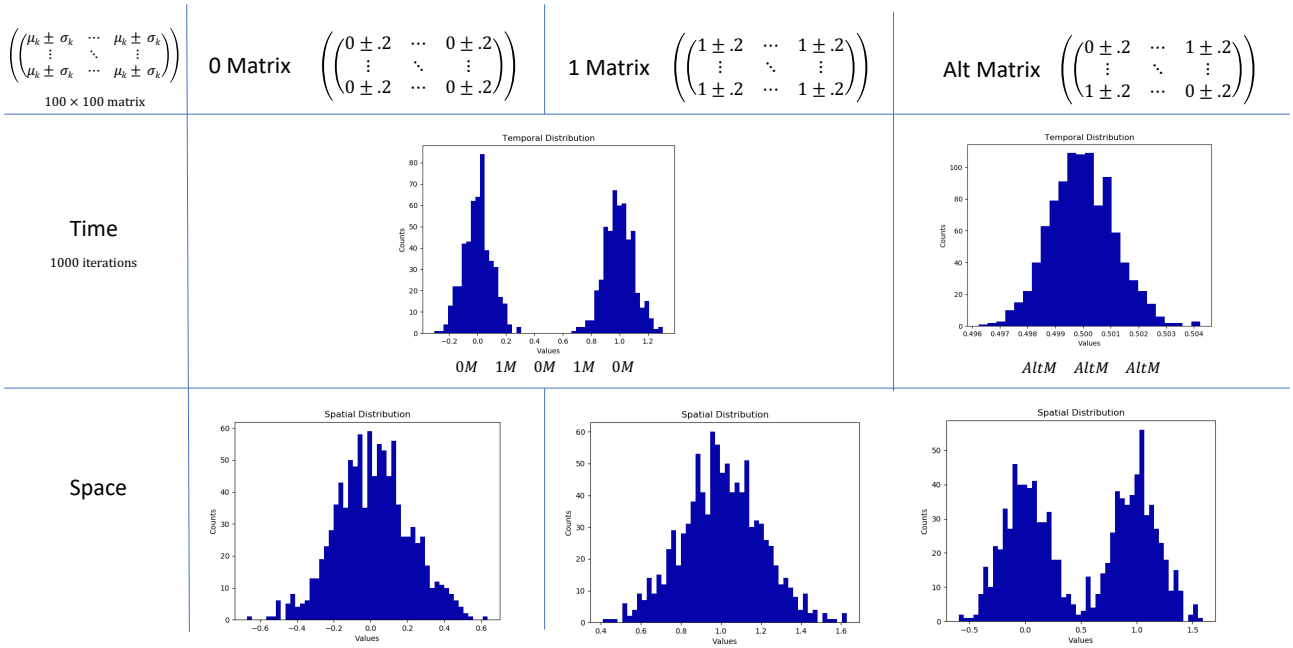

Figure 19: Figure shows the histograms of the matrices with respect to time and space.

First we created three different matrices. The first of these is called a 0-Matrix. As seen in Figure 19, the 0-Matrix is a 100×100 matrix with every element M_{ij} being a random variable with a mean 0 and a standard deviation of 0.2. We use this matrix to represent a room temperature equilibrium image as its basic properties are identical. Similarly, the 1-matrix

(random variables with mean of 1 and standard deviation of 0.2) accounts for a steady state image that shows no patterns even after a power is supplied (one giant hot plume). Finally, the Alt-Matrix, is a 100×100 matrix with four quadrants, each quadrant being a 0-Matrix or 1-Matrix alternatively as seen in Figure 19. This matrix represents an image that shows patterns and is at non-equilibrium steady state. We do this because we know that when we look at the hot or cold plumes separately, they should be normally distributed (Figure 10). This is how we can represent the Rayleigh-Bénard Convection mathematically using matrices. Although in reality it is much more complex than this, this is just the initial developments we made.

Spatially, the histograms show an obvious peak at 0 for the 0-Matrix, 1 for the 1 Matrix and two different peaks at 0 and 1 for the Alt-Matrix, similar to the Rayleigh-Bénard Convection distributions. Temporally, we arranged the matrices in two different ways. The first was the sequence of the 0-Matrix and 1-Matrix alternatively for a 1000 times. This essentially meant having a hot plume and then a cold plume in repeat or continuous form. We modelled this after similar studies that were conducted in the temporal analysis section in Rayleigh-Bénard Convection, as seen in figure 15 [a][c]. Figure 15[b] can be arrived at by using the Alt-Matrix. The role of the Alt-Matrix is to mimic a steady state image with patterns. By running the experiment a 1000 times, we can get the distribution of the Random Value Matrix over time. Since the mean of an image is close to 0.5 and due to the overall nature of the Alt-Matrix, we get a normally distributed histogram even though half the values are vastly different just like in the hot and cold sections of the convection patterns from Figure 15[b].

Further studies into the autocorrelation function being applied on this have shown that the idea could be taken on and variables like Shannon's Entropy can be calculated some day. The reason for this method is purely to see if the flow of information through a pixel/region can be modelled especially since the section can be adopted as either being hot(1) or cold(0). However more work would need to be added to see how to precisely model an information matrix and how one could extract useful information from it.

6 Conclusion

Although far-from-equilibrium systems are still hard to study and the theories for them are not fully developed, they can still be modelled using novel techniques within a wide array of experimental, computational and analytical approaches. While this is the case, there is still plenty of work to be done in non-equilibrium thermodynamics and we strongly believe that the techniques and ideas highlighted in this report will not only serve as evidence of reproducibility, but also engage the scientific community to explore more efficient and innovative ways to study such systems [21].

The use of the Rayleigh-Bénard Convection as a prototype system was proposed not because it is one of the oldest and most widely studied Canonical examples but because it is the easiest to reproduce and analyze [26, 13]. Due to this factor, there has been a considerable amount of work done with respect to the fluid mechanics aspects of the system but from a more thermodynamic perspective, many of the insights have gone unnoticed [35, 8].

In this report and in other published papers by the group, we have highlighted the importance of studying such systems and also discussed in great detail the computational and statistical approaches we used to perform a first principles thermodynamics study on the non-turbulent steady state Rayleigh-Bénard Convection when driven out-of-equilibrium [2]. Specifically we spent most of the time trying to understand the emergence of order that occurs in the form of patterns in the Rayleigh-Bénard Convection system.

With the appearance of patterns as the system is driven out-of-equilibrium, the statistics of the Rayleigh-Bénard Convection show a bifurcation from randomly distributed thermal fluctuations to a skewed bi-modal fluctuation distribution. The analysis shows how the steady state thermal images display local equilibrium like regions that coexist spatially. As the system moves from a room temperature equilibrium to a steady state non-equilibrium, an unexpected drop in standard deviation marks the onset of convective patterns suggesting that there is an underlying time independent character. Insightful as the statistics in space are, we see that the system does not behave uniformly across space and time which means that symmetry is broken and the system is non-ergodic [13, 21].

Other properties of our analysis of Rayleigh-Bénard Convection explain the ordering of the convective cells by indicating the presence of localized regions of hot and cold plumes and describing the spatial variation of their temperature manifold (as seen in Figure 10). From the various results we have obtained, its clear that in order to interpret non-equilibrium systems we must not only include the emergence of order in the form of thermodynamic variables but also consider temperature not as a state variable but as a function of the energy landscape [5].

Throughout the report, we have employed computational techniques using languages like Python, MATLAB and ImageJ. These techniques have formed the backbone of our statistical analysis approach and paved the way for all sorts of ideas that can be incorporated to further our understanding of these systems. Although the field is still a "work in progress", the present work provides some intuition as to how the systems behave the way they do and what can be done to advance our understanding of them [34].

7 Acknowledgements

This work was supported by the Department of Physics and Mechanical Engineering at Worcester Polytechnic Institute. The author is grateful and indebted to Germano Iannacchione, Atanu Chatterjee and Robert Daniello for advice and help in the development and analysis of the experimental and computational work done in this report. Atanu Chatterjee also upgraded the figures to make them look more visually representative. Manufacturing of the setup could not have been carried out without the help of Matt Ryder and Ian Anderson in the Mechanical Engineering Department.

8 Supplementary Files

- Circle.m - Matlab File for Extracting Circular Profile Statistics from Matrices (RBC)
- .SLDPRT and .SLDASM - CAD Files for Experimental Setup
- .esp files - CAM Files for Mini Mill (Manufacturing)
- Autocorrelation.py - Wiener-Khinchin theorem
- EqCorrelation.py - Random Value Generator for Matrices

References

[1] Chatterjee, A. Thermodynamics of action and organization in a system. *Complexity 21*, S1 (2016), 307–317.

[2] Chatterjee, A., and Iannacchione, G. The many faces of far-from-equilibrium thermodynamics: Deterministic chaos, randomness, or emergent order? *MRS Bulletin 44*, 2 (2019), 130–133.

[3] Chatterjee, A., Manohar, M., and Ramadurai, G. Statistical analysis of bus networks in india. *PloS one 11*, 12 (2016).

[4] Chatterjee, A., Mears, N., Yadati, Y., and Iannacchione, G. An overview of emergent order in far-from-equilibrium driven systems: From kuramoto oscillators to rayleigh-b\'enard convection. *arXiv preprint arXiv:1912.08385* (2019).

[5] Chatterjee, A., Yadati, Y., Mears, N., and Iannacchione, G. Coexisting ordered states, local equilibrium-like domains, and broken ergodicity in a non-turbulent rayleigh-bénard convection at steady-state. *Scientific reports 9*, 1 (2019), 1–11.

[6] Clausius, R. Über eine veränderte form des zweiten hauptsatzes der mechanischen wärmetheorie. *Annalen der Physik 169*, 12 (1854), 481–506.

[7] Cross, M. C., and Hohenberg, P. C. Pattern formation outside of equilibrium. *Reviews of modern physics 65*, 3 (1993), 851.

[8] Du, Y.-B., and Tong, P. Turbulent thermal convection in a cell with ordered rough boundaries. *Journal of Fluid Mechanics 407* (2000), 57–84.

[9] Du, Y.-B., and Tong, P. Temperature fluctuations in a convection cell with rough upper and lower surfaces. *Physical Review E 63*, 4 (2001), 046303.

[10] Gallavotti, G. Ergodicity: a historical perspective. equilibrium and nonequilibrium. *The European Physical Journal H 41*, 3 (2016), 181–259.

[11] Georgiev, G. Y., and Chatterjee, A. The road to a measurable quantitative understanding of self-organization and evolution. In *Evolution and Transitions in Complexity*. Springer, 2016, pp. 223–230.

[12] Gibbs, J. W. *The scientific papers of J. Willard Gibbs*, vol. 1. Longmans, Green and Company, 1906.

[13] Jaeger, H. M., and Liu, A. J. Far-from-equilibrium physics: An overview. *arXiv preprint arXiv:1009.4874* (2010).

[14] Jou, D., Casas-Vazquez, J., and Lebon, G. Extended irreversible thermodynamics revisited (1988-98). *Reports on Progress in Physics 62*, 7 (1999), 1035.

[15] Kadanoff, L. P. Turbulent heat flow: structures and scaling. *Physics today 54*, 8 (2001), 34–39.

[16] Kirkpatrick, T., Cohen, E., and Dorfman, J. Fluctuations in a nonequilibrium steady state: Basic equations. *Physical Review A 26*, 2 (1982), 950.

[17] Kolmogorov, A. Lokalnaja struktura turbulentnosti v neschtschimaemoi schidkosti pri otschen bolschich tschislach reynoldsa (the local structure of turbulence in incompressible viscous fluid for very large reynolds numbers). In *Dokl. AN SSSR* (1941), vol. 30, pp. 299–303.

[18] Koschmieder, E. L. *Bénard cells and Taylor vortices*. Cambridge University Press, 1993.

[19] Lebowitz, J. L. Boltzmann's entropy and time's arrow. *Physics today 46* (1993), 32–32.

[20] Lieb, E. H. *Statistical Mechanics: Selecta of Elliott H. Lieb*. Springer Science & Business Media, 2013.

[21] Lucia, U. Stationary open systems: A brief review on contemporary theories on irreversibility. *Physica A: Statistical Mechanics and its Applications 392*, 5 (2013), 1051–1062.

[22] Martyushev, L. M., and Seleznev, V. D. Maximum entropy production principle in physics, chemistry and biology. *Physics reports 426*, 1 (2006), 1–45.

[23] Nicolis, G. Self-organization in nonequilibrium systems. *Dissipative Structures to Order through Fluctuations* (1977), 339–426.

[24] Pawar, S., and Sunnapwar, V. K. Experimental studies on heat transfer to newtonian and non-newtonian fluids in helical coils with laminar and turbulent flow. *Experimental Thermal and Fluid Science 44* (2013), 792–804.

[25] Planck, M. *Treatise on thermodynamics*. Courier Corporation, 2013.

[26] Rayleigh, L. Lix. on convection currents in a horizontal layer of fluid, when the higher temperature is on the under side. *The London, Edinburgh, and Dublin Philosophical Magazine and Journal of Science 32*, 192 (1916), 529–546.

[27] Shannon, C. E. A mathematical theory of communication. *Bell system technical journal 27*, 3 (1948), 379–423.

[28] Srinivasarao, M., Iannacchione, G. S., and Parikh, A. N. Biologically inspired far-from-equilibrium materials. *MRS Bulletin 44*, 2 (2019), 91–95.

[29] Stevens, R. J., Lohse, D., and Verzicco, R. Prandtl and rayleigh number dependence of heat transport in high rayleigh number thermal convection. *Journal of fluid mechanics 688* (2011), 31–43.

[30] Verma, M. K. Asymmetric energy transfers in driven nonequilibrium systems and arrow of time. *The European Physical Journal B 92*, 9 (2019), 190.

[31] Vilar, J. M., and Rubi, J. Thermodynamics "beyond" local equilibrium. *Proceedings of the National Academy of Sciences 98*, 20 (2001), 11081–11084.

[32] Wiener, N., et al. Generalized harmonic analysis. *Acta mathematica 55* (1930), 117–258.

[33] Yadati, Y., McGrath, S., Chatterjee, A., Georgiev, G., and Iannacchione, G. A detailed thermodynamic study of rayleigh-benard cells. *Bulletin of the American Physical Society 63* (2018).

[34] Yadati, Y., Mears, N., and Chatterjee, A. Spatio-temporal characterization of thermal fluctuations in a non-turbulent rayleigh–bénard convection at steady state. *Physica A: Statistical Mechanics and its Applications* (2019), 123867.

[35] Zhou, Q., and Xia, K.-Q. Thermal boundary layer structure in turbulent rayleigh–bénard convection in a rectangular cell. *Journal of Fluid Mechanics 721* (2013), 199–224.